INSTITUTE OF PHYSICS PUBLISHING PHYSICS IN MEDICINE AND BIOLOGY

Phys. Med. Biol. **48** (2003) 1971–1986 PII: S0031-9155(03)60835-3

Three-dimensional forward solver and its performance analysis for magnetic resonance electrical impedance tomography (MREIT) using recessed electrodes

Byung Il Lee[1], Suk Hoon Oh[2], Eung Je Woo[1], Soo Yeol Lee[2], Min Hyoung Cho[2], Ohin Kwon[3], Jin Keun Seo[4], June-Yub Lee[5] and Woon Sik Baek[1]

[1] College of Electronics and Information, Kyung Hee University, Korea
[2] Graduate School of East-West Medical Sciences, Kyung Hee University, Korea
[3] Department of Mathematics, Konkuk University, Korea
[4] Department of Mathematics, Yonsei University, Korea
[5] Department of Mathematics, Ewha Womans University, Korea

E-mail: ejwoo@khu.ac.kr

Received 14 March 2003
Published 17 June 2003
Online at stacks.iop.org/PMB/48/1971

Abstract

In magnetic resonance electrical impedance tomography (MREIT), we try to reconstruct a cross-sectional resistivity (or conductivity) image of a subject. When we inject a current through surface electrodes, it generates a magnetic field. Using a magnetic resonance imaging (MRI) scanner, we can obtain the induced magnetic flux density from MR phase images of the subject. We use recessed electrodes to avoid undesirable artefacts near electrodes in measuring magnetic flux densities. An MREIT image reconstruction algorithm produces cross-sectional resistivity images utilizing the measured internal magnetic flux density in addition to boundary voltage data. In order to develop such an image reconstruction algorithm, we need a three-dimensional forward solver. Given injection currents as boundary conditions, the forward solver described in this paper computes voltage and current density distributions using the finite element method (FEM). Then, it calculates the magnetic flux density within the subject using the Biot–Savart law and FEM. The performance of the forward solver is analysed and found to be enough for use in MREIT for resistivity image reconstructions and also experimental designs and validations. The forward solver may find other applications where one needs to compute voltage, current density and magnetic flux density distributions all within a volume conductor.

1. Introduction

Imaging cross-sectional resistivity (or conductivity) distributions of the human body has been a research goal in electrical impedance tomography (EIT) (Webster 1990, Boone *et al* 1997, Saulnier *et al* 2001). The measured data for this imaging technique are mostly boundary voltages on a set of surface electrodes due to multiple injection currents. Recently, magnetic resonance electrical impedance tomography (MREIT) has been suggested to overcome the ill-posedness of the image reconstruction problem in EIT (Zhang 1992, Woo *et al* 1994, Ider and Birgul 1998). Currently, MREIT research is making rapid progress in algorithm developments (Eyuboglu *et al* 2001, Kwon *et al* 2002a, 2002b, Birgul *et al* 2001, Ider *et al* 2003, Seo *et al* 2003a, 2003b) and also in experimental techniques (Birgul *et al* 2001, Khang *et al* 2002, Lee *et al* 2003). MREIT is very promising in that it provides cross-sectional resistivity images with a better accuracy and spatial resolution since it utilizes the internal magnetic flux density data due to injection currents. If we can reconstruct accurate static images of resistivity distributions using MREIT techniques, there will be numerous potential applications especially in functional imaging and neuronal source localization problems. Images from MREIT may also be used as *a priori* information in EIT image reconstructions for better results. The disadvantages of MREIT over EIT may include the lack of portability, potentially long imaging time and requirement of an expensive MRI scanner.

The injection current I during MR imaging distorts the MR phase image in such a way that the phase change is proportional to the component of the induced magnetic flux density $\mathbf{B}$ that is parallel to the direction of the main magnetic field of an MRI scanner. This means that we must rotate the subject inside the MRI scanner to obtain all three components of the induced magnetic flux density. After we measure all three components of $\mathbf{B} = (B_x, B_y, B_z)$, the internal current density distribution $\mathbf{J}$ can be obtained as $\mathbf{J} = \nabla \times \mathbf{B}/\mu_0$ where μ_0 is the magnetic permeability of the free space and biological tissues. Experimental methods of obtaining magnetic flux density and current density images are described by Joy *et al* (1989), Scott *et al* (1991), Gamba and Delpy (1998), Eyuboglu *et al* (1998), Gamba *et al* (1999) and Joy *et al* (1999).

When $\mathbf{B} = (B_x, B_y, B_z)$ is available, we can use $\mathbf{J}$ to reconstruct resistivity images using image reconstruction algorithms such as the J-substitution algorithm (Kwon *et al* 2002b, Khang *et al* 2002, Lee *et al* 2003), current-constrained-voltage-scaled-reconstruction algorithm (Birgul *et al* 2003) and equipotential line methods (Kwon *et al* 2002a, Ider *et al* 2003). There are different algorithms utilizing only one component of $\mathbf{B}$ such as B_z to avoid the subject rotation procedure (Seo *et al* 2003a, 2003b). Figure 1 shows a diagram of an MREIT system. Given a model of a subject with an assumed resistivity distribution, injection currents and electrode configurations, a three-dimensional forward solver computes distributions of voltage V, current density $\mathbf{J}$ and magnetic flux density $\mathbf{B}$ or only B_z. The measured and computed data for V, $\mathbf{B}$ (or B_z) and/or $\mathbf{J}$ are used to reconstruct cross-sectional resistivity images depending on the algorithm used.

Similar forward problems have been studied in EEG and MEG (Pruis *et al* 1993, Awada *et al* 1997, Gencer and Tanzer 1999a, Mosher *et al* 1999) and EIT (Vauhknonen *et al* 1999, Gencer and Tek 1999b, de Munck *et al* 2000, Polydorides and Lionheart 2002) using the finite element method (FEM) or boundary element method (BEM). Especially, Polydorides and Lionheart (2002) developed a software package called Electrical Impedance and Diffuse Optical Reconstruction Software (EIDORS) where a three-dimensional forward solver in EIT is nicely implemented. The forward problem in MREIT is, however, different from these problems since we should compute distributions of V, $\mathbf{J}$ and $\mathbf{B}$ all within an electrically conducting domain.

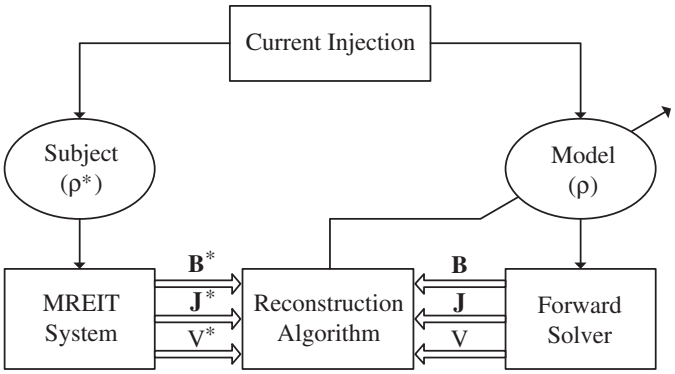

Figure 1. MREIT system block diagram. Resistivity, voltage, current density and magnetic flux density are denoted as ρ, V, $\mathbf{J}$ and $\mathbf{B}$, respectively. Quantities from the imaging subject are shown with superscripts $*$.

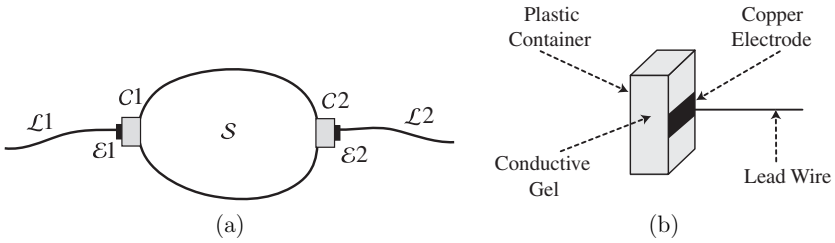

Figure 2. (a) Definition of domains and (b) recessed electrode assembly.

This paper describes a three-dimensional forward solver for the algorithm development and image reconstructions as well as the experimental design and verification in MREIT. After we define the forward problem in MREIT using recessed electrodes, we will describe numerical techniques adopted in our forward solver. We will also discuss the performance of the forward solver in achieving the required numerical accuracy. Solutions of the forward solver will be compared with the measured data using a 0.3 T experimental MREIT system and also with analytic solutions in a certain case where they are available.

2. Methods

2.1. Forward problem in MREIT using recessed electrodes

Let $\mathcal{S} \subset \mathbb{R}^3$ be an electrically conducting subject with its boundary $\partial\mathcal{S}$ as shown in figure 2(a). Two copper electrodes are denoted as $\mathcal{E}1$ and $\mathcal{E}2$ and lead wires are shown as $\mathcal{L}1$ and $\mathcal{L}2$. Both electrodes $\mathcal{E}1$ and $\mathcal{E}2$ are recessed from the surface of the subject $\partial\mathcal{S}$ by the plastic containers, $\mathcal{C}1$ and $\mathcal{C}2$, respectively. We define regions of containers, electrodes and lead wires as $\mathcal{C} = \mathcal{C}1 \cup \mathcal{C}2$, $\mathcal{E} = \mathcal{E}1 \cup \mathcal{E}2$ and $\mathcal{L} = \mathcal{L}1 \cup \mathcal{L}2$, respectively. Figure 2(b) shows the recessed electrode assembly. We fill the container with a gel of a known resistivity value. This kind of electrode assembly is desirable since it helps us in producing artefact-free MR images of the subject including its boundary. Due to the RF shielding effect of the copper electrode, severe artefacts are produced in MR images near the electrode. For example, Khang *et al* (2002) and Lee *et al* (2003) could reconstruct resistivity images from a saline phantom with surface copper electrodes only within a restricted internal region of the phantom due to

these artefacts. By recessing the electrode, we can effectively move this artefact away from the boundary $\partial\mathcal{S}$.

Now, we let $\mathcal{D}$ be the region including the subject and two plastic containers, that is, $\mathcal{D} = \mathcal{S} \cup \mathcal{C}$ with its boundary $\partial\mathcal{D}$. Assuming that we inject a current I through the pair of copper electrodes $\mathcal{E}1$ and $\mathcal{E}2$ attached to $\partial\mathcal{D}$, we can formulate the following boundary value problem with the Neumann boundary condition:

$$\begin{cases} \nabla\left[\frac{1}{\rho(\mathbf{r})}\nabla V(\mathbf{r})\right] = 0 & \text{in } \mathcal{D} \\ -\frac{1}{\rho}\nabla V \cdot \mathbf{n} = g & \text{on } \partial\mathcal{D} \end{cases} \tag{1}$$

where ρ and V are the resistivity and voltage distribution in $\mathcal{D}$, respectively, $\mathbf{n}$ is the outward unit normal vector on $\partial\mathcal{D}$ and g is the magnitude of the current density on $\partial\mathcal{D}$ due to the injection current I. A position vector in $\mathbb{R}^3$ is denoted as $\mathbf{r}$. Once we have found a numerical solution V of (1), we can compute the internal current density distribution $\mathbf{J}$ as

$$\mathbf{J}(\mathbf{r}) = -\frac{1}{\rho(\mathbf{r})}\nabla V(\mathbf{r}) \quad \text{in } \mathcal{D}. \tag{2}$$

We are interested in the magnetic flux density in $\mathcal{S}$ denoted as $\mathbf{B}$. For the purpose of numerical computations, we divide $\mathbf{B}$ into four components as

$$\mathbf{B}(\mathbf{r}) = \mathbf{B}_{\mathcal{S}}(\mathbf{r}) + \mathbf{B}_{\mathcal{C}}(\mathbf{r}) + \mathbf{B}_{\mathcal{E}}(\mathbf{r}) + \mathbf{B}_{\mathcal{L}}(\mathbf{r}) \quad \text{in } \mathcal{S} \tag{3}$$

where $\mathbf{B}_{\mathcal{S}}$, $\mathbf{B}_{\mathcal{C}}$, $\mathbf{B}_{\mathcal{E}}$ and $\mathbf{B}_{\mathcal{L}}$ are magnetic flux densities due to $\mathbf{J}$ in $\mathcal{S}, \mathcal{C}, \mathcal{E}$ and I in $\mathcal{L}$, respectively. From the Biot–Savart law, we have

$$\mathbf{B}_{\mathcal{X}}(\mathbf{r}) = \frac{\mu_0}{4\pi}\int_{\mathcal{X}} \mathbf{J}(\mathbf{r}') \times \frac{\mathbf{r}-\mathbf{r}'}{|\mathbf{r}-\mathbf{r}'|^3}\,\mathrm{d}v' \tag{4}$$

where $\mathcal{X}$ is $\mathcal{S}, \mathcal{C}$ or $\mathcal{E}$ and

$$\mathbf{B}_{\mathcal{L}}(\mathbf{r}) = \frac{\mu_0 I}{4\pi}\int_{\mathcal{L}} \mathbf{a}(\mathbf{r}') \times \frac{\mathbf{r}-\mathbf{r}'}{|\mathbf{r}-\mathbf{r}'|^3}\,\mathrm{d}l' \tag{5}$$

where $\mathbf{a}(\mathbf{r}')$ is the unit vector in the direction of the current flow at $\mathbf{r}' \in \mathcal{L}$. The magnetic flux density $\mathbf{B}$ must also satisfy the following equation:

$$\mathbf{J}_B(\mathbf{r}) = \frac{1}{\mu_0}\nabla \times \mathbf{B}(\mathbf{r}) \quad \text{in } \mathcal{S}. \tag{6}$$

For the compatibility of solutions, we must have

$$\mathbf{J}(\mathbf{r}) = \mathbf{J}_B(\mathbf{r}) \qquad \nabla \cdot \mathbf{J}(\mathbf{r}) = 0 \qquad \text{and} \qquad \nabla \cdot \mathbf{J}^B(\mathbf{r}) = 0 \quad \text{in } \mathcal{S}. \tag{7}$$

2.2. Effects of recessed electrodes and lead wires

Before we describe the numerical method of solving the forward problem in MREIT, we discuss the effects of recessed electrodes and lead wires on $\mathbf{B}$ and $\mathbf{J}$ in $\mathcal{S}$. We let $\Phi(\mathbf{r}, \mathbf{r}') = -\frac{1}{4\pi}\frac{1}{|\mathbf{r}-\mathbf{r}'|}$. Since $\nabla \cdot \mathbf{J} = 0$, we have

$$\begin{aligned} \frac{1}{\mu_0}\nabla \times \mathbf{B}_{\mathcal{S}}(\mathbf{r}) &= -\nabla \times \nabla \times \int_{\mathcal{S}} \Phi(\mathbf{r}, \mathbf{r}')\mathbf{J}(\mathbf{r}')\,\mathrm{d}v' \\ &= (-\nabla^2 + \nabla\nabla\cdot)\int_{\mathcal{S}} \Phi(\mathbf{r}, \mathbf{r}')\mathbf{J}(\mathbf{r}')\,\mathrm{d}v' \\ &= \mathbf{J}(\mathbf{r}) + \nabla\nabla \cdot \int_{\mathcal{S}} \Phi(\mathbf{r}, \mathbf{r}')\mathbf{J}(\mathbf{r}')\,\mathrm{d}v' \\ &= \mathbf{J}(\mathbf{r}) - \nabla \int_{\mathcal{S}} \nabla_{\mathbf{r}'} \cdot (\Phi(\mathbf{r}, \mathbf{r}')\mathbf{J}(\mathbf{r}'))\,\mathrm{d}v' \\ &= \mathbf{J}(\mathbf{r}) - \nabla \int_{\partial\mathcal{S}} \Phi(\mathbf{r}, \mathbf{r}')\mathbf{J}(\mathbf{r}') \cdot \mathbf{n}(\mathbf{r})\,\mathrm{d}s' \end{aligned} \tag{8}$$

for all $\mathbf{r}$ in $\mathcal{S}$ where $\mathbf{n}$ is the outward unit normal vector on $\partial\mathcal{S}$. With (3), (6) and (8), we get

$$\frac{1}{\mu_0}\nabla \times (\mathbf{B}_{\mathcal{C}}(\mathbf{r}) + \mathbf{B}_{\mathcal{E}}(\mathbf{r}) + \mathbf{B}_{\mathcal{L}}(\mathbf{r})) = \nabla \int_{\partial\mathcal{S}} \Phi(\mathbf{r}, \mathbf{r}')\mathbf{J}(\mathbf{r}') \cdot \mathbf{n}(\mathbf{r})\, \mathrm{d}s'. \tag{9}$$

This means that the current density $\mathbf{J}$ within $\mathcal{S}$ due to $\mathbf{B}_{\mathcal{C}}$, $\mathbf{B}_{\mathcal{E}}$ and $\mathbf{B}_{\mathcal{L}}$ is dependent only on the current density or Neumann boundary condition on $\partial\mathcal{S}$. Therefore, two totally different sets of recessed electrodes and lead wires produce the same current density $\mathbf{J}$ in $\mathcal{S}$ only if they provide the same Neumann boundary condition on $\partial\mathcal{S}$. The actual geometrical shape of $\mathcal{L}$ does not affect the computed $\mathbf{J}$ though the shape of $\mathcal{C}$ may have some effects since it can influence the Neumann boundary condition on $\partial\mathcal{S}$.

Note that the magnetic flux density $\mathbf{B}$ in $\mathcal{S}$ will be different depending on the shapes and dimensions of recessed electrodes and lead wires. However, we have

$$\nabla^2(\mathbf{B}_{\mathcal{C}}(\mathbf{r}) + \mathbf{B}_{\mathcal{E}}(\mathbf{r}) + \mathbf{B}_{\mathcal{L}}(\mathbf{r})) = 0 \tag{10}$$

since $\nabla^2 \frac{1}{|\mathbf{r}-\mathbf{r}'|} = 0$ when $\mathbf{r} \neq \mathbf{r}'$. We may utilize (10) to remove the effects of recessed electrodes and lead wires from the measured $\mathbf{B}$ in $\mathcal{S}$ in some image reconstruction algorithms (Seo *et al* 2003a, 2003b).

2.3. Computation of voltage V and current density $\mathbf{J}$

We use FEM to numerically solve (1). We first construct a three-dimensional model of $\mathcal{D}$ and $\mathcal{E}$. We assume that the thickness of each electrode is negligibly thin. For the discretization of the model into a finite element mesh, we use eight-node hexahedral elements with trilinear interpolation functions ψ_i for $i = 1, \ldots, 8$. For the standard hexahedral element of $[-1, 1]^3$,

$$\psi_i = \tfrac{1}{8}(1 + xx_i)(1 + yy_i)(1 + zz_i) \qquad i = 1, \ldots, 8$$

where x_i, y_i and z_i are the local coordinates of the ith nodal point of the element.

The current density distribution underneath each electrode is not uniform in most cases. This means that we only know the amount of injection current I without knowing the Neumann boundary condition g in (1). Therefore, assuming that each electrode is an equipotential surface due to its high conductivity, we first solve the following boundary value problem with mixed boundary conditions:

$$\begin{cases} \nabla\big[\frac{1}{\rho(\mathbf{r})}\nabla\tilde{V}(\mathbf{r})\big] = 0 \quad \text{in } \mathcal{D} \\ \tilde{V} = 1 \quad \text{on } \partial\mathcal{D}_{\mathcal{E}1} \qquad \text{and} \qquad \tilde{V} = 0 \quad \text{on } \partial\mathcal{D}_{\mathcal{E}2} \\ -\frac{1}{\rho}\nabla\tilde{V} \cdot \mathbf{n} = 0 \quad \text{on } \partial\mathcal{D} \setminus (\partial\mathcal{D}_{\mathcal{E}1} \cup \partial\mathcal{D}_{\mathcal{E}2}) \end{cases} \tag{11}$$

where $\partial\mathcal{D}_{\mathcal{E}1} = \overline{\mathcal{D}} \cap \overline{\mathcal{E}1}$ and $\partial\mathcal{D}_{\mathcal{E}2} = \overline{\mathcal{D}} \cap \overline{\mathcal{E}2}$ are the portions of $\partial\mathcal{D}$ contacting the electrodes $\mathcal{E}1$ and $\mathcal{E}2$, respectively. Following the standard procedure of FEM (Burnett 1987), we compute the numerical solution of $\tilde{V}$ in (11). This solution is a set of nodal voltages of the corresponding finite element mesh. Expressing the voltage at a position within an element of the mesh as a linear combination of eight nodal voltages of the element and interpolation functions, we can compute $\tilde{\mathbf{J}}$ from (2) with $\tilde{V}$ instead of V. We now compute the total current $\tilde{I}$ passing through the boundary $\partial\mathcal{D}_{\mathcal{E}1}$. Then, we multiply the computed voltage $\tilde{V}$ and current density $\tilde{\mathbf{J}}$ by $I/\tilde{I}$. This gives us the numerical solution V of (1) and $\mathbf{J}$ of (2) due to the injection current I.

2.4. Computation of magnetic flux density $\mathbf{B}$ using the Biot–Savart law

As described before, we are interested in the magnetic flux density only inside the subject $\mathcal{S}$. We now describe how to compute each term on the right-hand side of (3) using the Biot–Savart

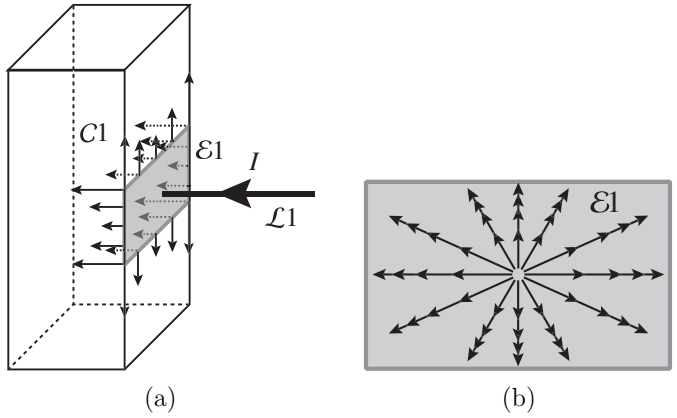

Figure 3. (a) Out-of-plane source and sink currents on the electrode $\mathcal{E}1$ and (b) surface current density within the electrode.

law. In the next section, we will introduce a faster method of computing $\mathbf{B}$ in $\mathcal{S}$ using FEM. However, since the method based on FEM requires the computation of $\mathbf{B}$ on $\partial\mathcal{S}$ as a boundary condition, the method described in this section will also be utilized in the next section.

2.4.1. Computation of $\mathbf{B}_{\mathcal{S}}$ *and* $\mathbf{B}_{\mathcal{C}}$. Assuming that $\mathbf{J}$ does not change much within each element of the mesh for $\mathcal{S}$, we compute $\mathbf{B}_{\mathcal{S}}$ as

$$\mathbf{B}_{\mathcal{S}}(\mathbf{r}) = \frac{\mu_0}{4\pi} \sum_{e=1}^{NE_{\mathcal{S}}} \mathbf{J}_c^{(e)} \times \frac{\mathbf{r} - \mathbf{r}_c^{(e)}}{\left|\mathbf{r} - \mathbf{r}_c^{(e)}\right|^3} \Delta v^{(e)} \tag{12}$$

where $NE_{\mathcal{S}}$ is the number of elements, $\mathbf{r}_c^{(e)}$ the centre point of the eth element, $\mathbf{J}_c^{(e)}$ the current density at $\mathbf{r}_c^{(e)}$ and $\Delta v^{(e)}$ the volume of the element in the finite element mesh of $\mathcal{S}$. In order to avoid the singularity where $\mathbf{r} = \mathbf{r}_c^{(e)}$, we compute $\mathbf{B}_{\mathcal{S}}$ at all nodal points of the mesh. Since we have already computed $\mathbf{J}$ in $\mathcal{C}$ from the numerical solution of (1) and (2), we can calculate $\mathbf{B}_{\mathcal{C}}$ in the same way as in (12).

2.4.2. Computation of $\mathbf{B}_{\mathcal{E}}$. The magnetic flux density $\mathbf{B}_{\mathcal{E}}$ in $\mathcal{S}$ is due to the surface current in $\mathcal{E}$. We first choose the electrode $\mathcal{E}1$ in figure 3(a) which illustrates the current flowing into $\mathcal{E}1$ from $\mathcal{L}1$ and currents leaving $\mathcal{E}1$ into $\mathcal{C}1$. Considering $\mathcal{E}1$ as a two-dimensional domain with a high conductivity value, we construct a two-dimensional finite element mesh for $\mathcal{E}1$. From the computed current density $\mathbf{J}$ on $\partial\mathcal{D}_{\mathcal{E}1} = \overline{\mathcal{D}} \cap \overline{\mathcal{E}1}$ in section 2.3, we can compute the sink currents on all nodes of the finite element mesh. The injection current I from the lead wire becomes a source current at the centre node of the mesh.

To calculate the surface current density shown in figure 3(b), we solve the following two-dimensional boundary value problem in $\mathcal{E}1$:

$$\begin{cases} \nabla^2 V(\mathbf{r}) = f & \text{in } \mathcal{E}1 \\ \nabla V \cdot \mathbf{n} = 0 & \text{on } \partial\mathcal{E}1 \end{cases} \tag{13}$$

where f is the source or sink current. From the numerical solution of (13) using FEM, we can easily compute the surface current density on $\mathcal{E}1$. After we repeat the computation for $\mathcal{E}2$, we can calculate $\mathbf{B}_{\mathcal{E}}$ in a similar way as in (12).

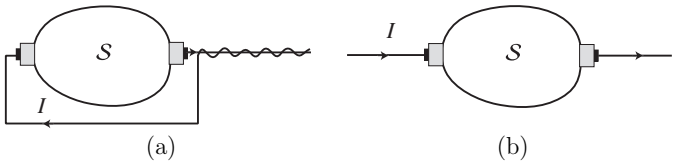

Figure 4. Lead wire geometry. (a) Twisted wires and (b) straight wires.

2.4.3. Computation of $\mathbf{B}_{\mathcal{L}}$. We note that the computation of $\mathbf{B}_{\mathcal{L}}$ requires the information on the actual geometrical shape of lead wires. We consider two cases shown in figure 4. In figure 4(a), we should include the correct geometry of the portion of lead wires where they are not twisted together. In figure 4(b), the lead wires run straight in one direction within a certain range. Note that the current I in a portion of lead wires far away from $\mathcal{S}$ has a negligible effect on the magnetic flux density in $\mathcal{S}$. In either case, we can numerically compute (5) by discretizing the lead wires into many small line segments. For the lead wire shown in figure 4(b), one might use an analytic solution for $\mathbf{B}_{\mathcal{L}}$. Long and straight lead wires in the z direction may be desirable for measuring B_z in $\mathcal{S}$ since only the currents in the x and y directions determine B_z.

2.5. Computation of magnetic flux density $\mathbf{B}$ *using FEM*

Numerical calculation of the magnetic flux density $\mathbf{B}$ using the Biot–Savart law requires a large amount of computation time since it is in the form of three-dimensional convolution. In this section, we introduce a faster method using FEM. We first note that

$$\nabla^2\mathbf{B} = -\mu_0\nabla\times\mathbf{J} \quad \text{in } \mathcal{S}. \tag{14}$$

Since $\mathbf{J}$ is available from (2), we can solve (14) for $\mathbf{B}$ using FEM if the boundary conditions of $\mathbf{B}$ are known on $\partial\mathcal{S}$. We, therefore, compute $\mathbf{B} = \mathbf{B}_{\mathcal{S}} + \mathbf{B}_{\mathcal{C}} + \mathbf{B}_{\mathcal{E}} + \mathbf{B}_{\mathcal{L}}$ using the methods described in the previous section only for $\mathbf{r} \in \partial\mathcal{S}$. Then, we have the Dirichlet boundary condition on $\partial\mathcal{S}$ and can numerically solve (14) for $\mathbf{B}$ using FEM. Note that it is important to compute all four components of $\mathbf{B}$ on $\partial\mathcal{S}$ to find the appropriate Dirichlet boundary condition of $\mathbf{B}$ in (14). We can also compute (14) in any three-dimensional subdomain of $\mathcal{S}$ as long as we correctly calculate its boundary condition.

2.6. Computation of current density $\mathbf{J}_B$ *from magnetic flux density*

With the computed magnetic flux density $\mathbf{B}$, we can calculate $\mathbf{J}_B$ in (6). Since we have computed the magnetic flux density on all nodal points in $\mathcal{S}$, we can express the magnetic flux density at a position within an element of the mesh using eight nodal values of $\mathbf{B}$ and interpolation functions. Then, the curl operation in (6) can be performed without numerical differentiations as in the computation of (2).

2.7. Numerical implementation

As shown in figure 5(a), we assumed a cubic subject of $50 \times 50 \times 50$ mm^3 with an isotropic and piecewise constant resistivity distribution ρ. We used the cubic subject to compare the forward solver with experimental results using a cubic phantom. The cubic phantom was used in experiments for the ease of subject rotations to measure all three components of $\mathbf{B}$. The origin was located at the centre of the subject in figure 5(a). Figures 5(b)–(e) show four

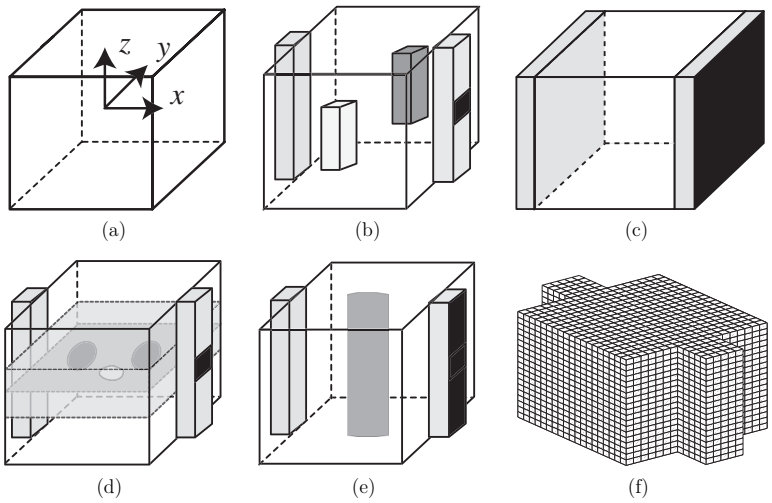

Figure 5. (a) Cubic subject of $50 \times 50 \times 50$ mm^3 with an isotropic and piecewise constant resistivity distribution. (b) Model with narrow recessed electrodes for the analysis of numerical accuracy. (c) Homogeneous model with full-size recessed electrodes for the comparison with analytic solutions. (d) Thorax model and (e) model containing a cylindrical object with narrow recessed electrodes. (f) Picture of a typical finite element mesh using hexahedral elements.

different models of the subject with recessed electrodes. We assumed the lead wire geometry in figure 4(b) only for simplicity in numerical computations. The model in figure 5(c) includes two full-size recessed electrodes ($10 \times 50 \times 50$ mm^3) covering the entire areas of two surfaces. The other three models in figures 5(b), (d) and (e) are equipped with two narrow recessed electrodes ($10 \times 5 \times 50$ mm^3).

We used the model in figure 5(b) to determine the finite element mesh with a desirable numerical accuracy. The homogeneous model in figure 5(c) with full-size recessed electrodes was used to compare the numerical results with analytic solutions. We used the thorax model in figure 5(d) to present typical numerical results of the three-dimensional forward solver. The model in figure 5(e) was for the comparison between the numerical and experimental results. The amount of injection current was 1 mA for the models in figures 5(b)–(d) and 28 mA for (e). Figure 5(f) shows a picture of a typical finite element mesh using hexahedral elements.

We performed all computations using a PC with an Athlon 2000+ processor, 1 GB RAM and Windows 2000 Professional operating system. We used double precision floating point variables. For all numerical results, we checked the compatibility conditions in (7).

2.8. Experimental method for measuring magnetic flux density

In order to compare the computed magnetic flux density with the measured one, we acquired the magnetic flux density data following the procedure described by Khang *et al* (2002) and Lee *et al* (2003). We used our 0.3 T experimental MRI system with 25 cm bore. We manufactured a cubic phantom ($50 \times 50 \times 50$ mm^3, acrylic plastic) of the model in figure 5(e). The phantom was filled with a solution containing NaCl and $CuSO_4 \cdot 5H_2O$. The resistivity of the solution was 50 Ω cm. The cylindrical object at the centre of the phantom was made of agar with resistivity 300 Ω cm. We used two narrow recessed copper electrodes ($10 \times 5 \times 50$ mm^3) through which we injected a current of 28 mA. We set up the lead wires so that their shape was as close as possible to the model in figure 4(b). We captured phase images of the phantom

Table 1. Meshes with different numbers of elements and their relative numerical errors. Number of elements exclude the elements belonging to the recessed electrode assemblies.

Mesh index (m)	Number of elements ($X \times Y \times Z$)	ε_V^m (%)	ε_B^m (%)
1	1000 ($10 \times 10 \times 10$)	3.91	5.90
2	8000 ($20 \times 20 \times 20$)	1.66	2.31
3	27 000 ($30 \times 30 \times 30$)	1.04	1.35
4	64 000 ($40 \times 40 \times 40$)	0.751	0.944
5	216 000 ($60 \times 60 \times 60$)	0.481	0.581
6	1 728 000 ($120 \times 120 \times 120$)	NA	NA

using a standard spin echo pulse sequence synchronized with injection current pulses. Khang *et al* (2002) and Lee *et al* (2003) describe the experimental procedure and data processing method in detail and similar techniques are described by Joy *et al* (1989), Scott *et al* (1991), Gamba and Delpy (1998), Eyuboglu *et al* (1998) and Gamba *et al* (1999).

3. Results

3.1. Numerical accuracy, mesh size and computation time

In this section, we choose the model in figure 5(b). The resistivity distribution of the model was

$$\rho(x, y, z) = \begin{cases} 200\,\Omega\,\text{cm} & \text{for} \quad -15 \leqslant x \leqslant -5 \quad -15 \leqslant y \leqslant -5 \quad -15 \leqslant z \leqslant 5\,\text{mm} \\ 50\,\Omega\,\text{cm} & \text{for} \quad 5 \leqslant x \leqslant 15 \quad 5 \leqslant y \leqslant 15 \quad -5 \leqslant z \leqslant 15\,\text{mm} \\ 100\,\Omega\,\text{cm} & \text{otherwise.} \end{cases}$$

This resistivity distribution has no symmetry in all three directions. The resistivity within two containers of recessed electrodes was 100 Ω cm. To determine the fineness of a finite element mesh required for the numerical accuracy of the forward solver, we constructed six meshes in table 1 with different numbers of elements. We chose numbers 120, 60, 40, 30, 20 and 10 so that there are common nodes among different meshes.

We introduced two different methods of computing **B** in sections 2.4 and 2.5. In order to compare them, we computed **B** in $\mathcal{S}$ using the two methods with the meshes in table 1 and found that there is no significant difference in the numerical results except for computation times. Since the computation time of the method based on the Biot–Savart law described in section 2.4 was considerably longer, we decided to use the method based on FEM described in section 2.5.

Since the measured data in MREIT are the boundary voltage and internal magnetic flux density, we examined the numerical accuracy in the computed V and **B**. In table 1, m denotes the index of the mesh. We define the relative numerical error of the mth mesh over the $(m+1)$th mesh as

$$\varepsilon_V^m = \frac{\sqrt{\sum_{n=1}^{N} |V^{(m+1)}(\mathbf{r}_n) - V^m(\mathbf{r}_n)|^2}}{\sqrt{\sum_{n=1}^{N} |V^{(m+1)}(\mathbf{r}_n)|^2}} \times 100\,(\%)$$

where N is the number of nodal points common to both meshes, $\mathbf{r}_n$ is the nth common nodal point and $V^{(m+1)}$ and V^m are the computed voltages from the $(m+1)$th and mth meshes, respectively. Similarly, we can define ε_B^m. Table 1 shows the values of ε_V^m and ε_B^m.

We assumed that the error in the measured voltage V is larger than 0.1% (Boone *et al* 1997). From the sensitivity analysis by Scott *et al* (1992), we assumed that the amount of noise in the measured magnetic flux density **B** is greater than 0.1×10^{-9} T in most cases.

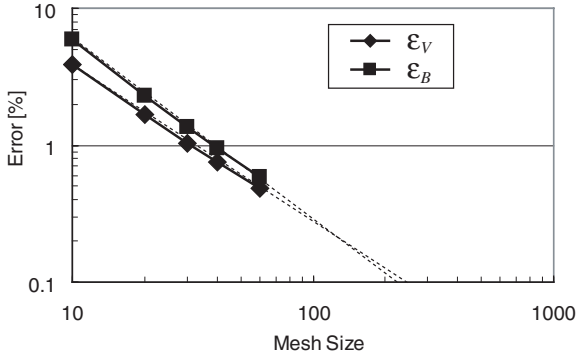

Figure 6. Log–log plot of numerical errors as a function of mesh size.

Table 2. Computation times of V, $\mathbf{J}$, $\mathbf{B}$ and $\mathbf{J}_B$ using a PC with an Athlon 2000+ processor, 1 GB RAM and Windows 2000 Professional operating system. We computed V on all nodes, $\mathbf{J}$ in all elements, $\mathbf{B}$ on the nodes of three planes and $\mathbf{J}_B$ in the elements of two layers. $T(\mathbf{B})^1$ is the computation time for $\mathbf{B}$ using the method described in section 2.4 and $T(\mathbf{B})^2$ is the corresponding computation time using the method based on FEM described in section 2.5.

Number of elements ($X \times Y \times Z$)	$T(V)$ (s)	$T(\mathbf{J})$ (s)	$T(\mathbf{B})^1$ (s)	$T(\mathbf{B})^2$ (s)	$T(\mathbf{J}_B)$ (s)
1000 ($10 \times 10 \times 10$)	0.2	0.016	0.14	0.016	$\approx$0
8000 ($20 \times 20 \times 20$)	2.8	0.13	3.2	0.094	0.062
27 000 ($30 \times 30 \times 30$)	16	0.39	21	0.19	0.094
64 000 ($40 \times 40 \times 40$)	44	1.0	88	0.33	0.16
216 000 ($60 \times 60 \times 60$)	240	3.4	645	0.80	0.38
512 000 ($80 \times 80 \times 80$)	760	8.2	2700	1.6	0.62
1728 000 ($120 \times 120 \times 120$)	3700	28	19 500	11	1.5

Dividing this by the average value of the computed $|\mathbf{B}|$ due to the injection current of 1 mA, we could get about 1.88% error in the measured $\mathbf{B}$. From the log–log plot of relative errors in figure 6, we decided to use a mesh with $80 \times 80 \times 80$ elements (total 512 000 elements and 531 441 nodes) for all computations in the subsequent sections. Figure 6 indicates that we may expect an error of about 0.4% for both ε_V and ε_B with this mesh. Using the sixth mesh with $120 \times 120 \times 120$ elements, we may obtain less than 0.1% error. However, the computation time using the sixth mesh was very long for the PC used in this paper. Table 2 shows the required computation times for calculations of V, $\mathbf{J}$, $\mathbf{B}$ and $\mathbf{J}_B$. Note that we computed V on all nodes, $\mathbf{J}$ in all elements, $\mathbf{B}$ on the nodes of three planes and $\mathbf{J}_B$ in the elements of two layers.

3.2. Comparison with analytic solutions

For the homogeneous model with resistivity 100 Ω cm and full-size recessed electrodes in figure 5(c), the computed voltage changed linearly only along the x direction with values of 28 mV at $x = -35$ mm (on the left copper electrode) and 0 V at $x = 35$ mm (on the right copper electrode). The error between the computed and theoretical voltage values was zero. The current density $\mathbf{J}$ in (2) was computed as $\mathbf{J} = (40, 10^{-7}, 10^{-8})\ \mu\text{A cm}^{-2}$ with a negligibly small error compared with the theoretical value of $\mathbf{J} = (40, 0, 0)\ \mu\text{A cm}^{-2}$. For the compatibility test in (7), we define the following three indices of

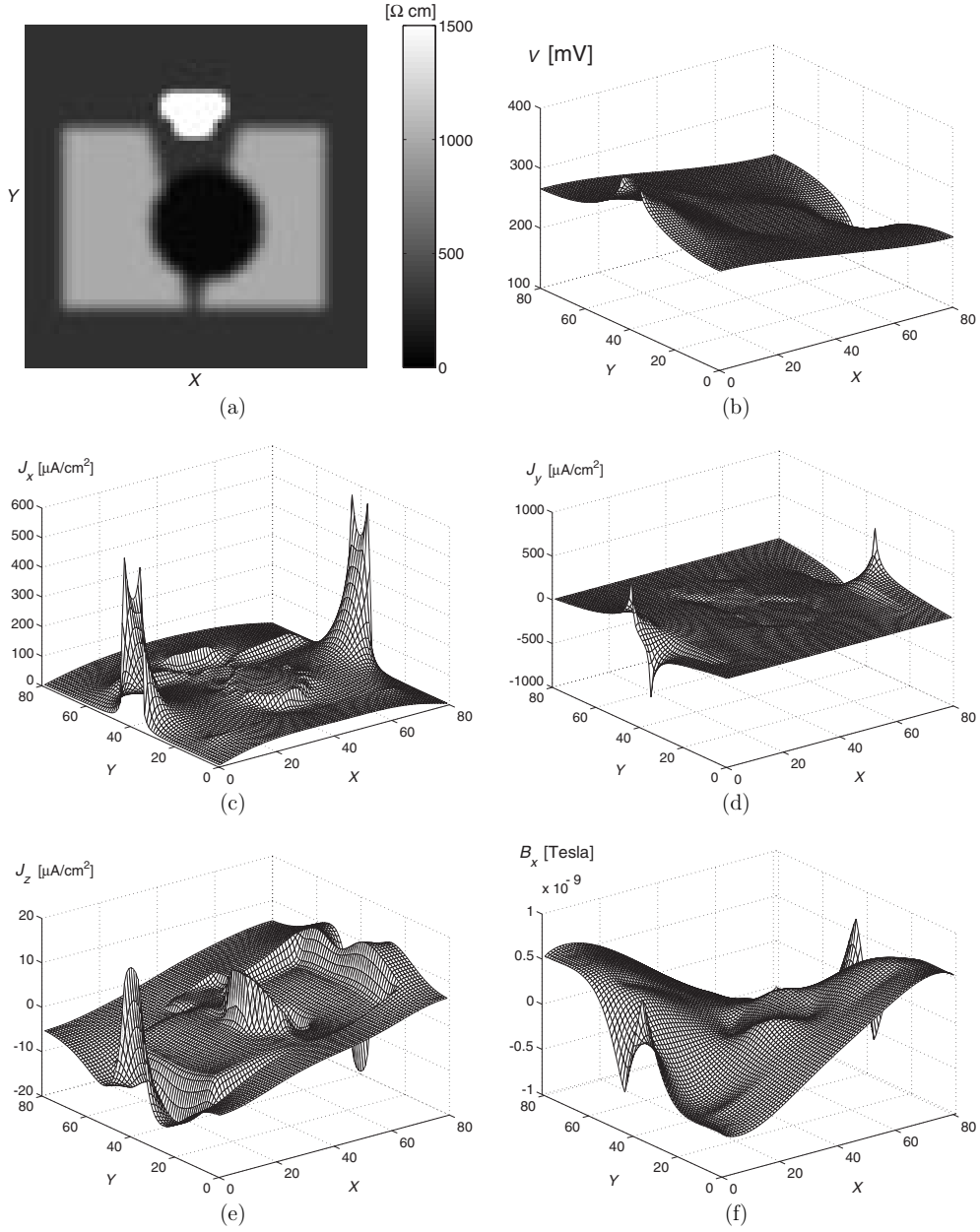

Figure 7. Typical numerical results for the thorax model in figure 5(d) with an injection current of 1 mA. (a) Resistivity distribution of the thorax model. Computed results of (b) V, (c) J_x, (d) J_y, (e) J_z, (f) B_x, (g) B_y and (h) B_z.

$$\varepsilon_{J_B} = \frac{\|\mathbf{J} - \mathbf{J}_B\|_2}{\|\mathbf{J}\|_2} \times 100\,(\%)$$

$$\varepsilon_{\nabla\cdot\mathbf{J}} = \frac{\|\nabla \cdot \mathbf{J}\|_2 \Delta p}{\|\mathbf{J}\|_2} \times 100 \qquad \text{and} \qquad \varepsilon_{\nabla\cdot\mathbf{J}_B} = \frac{\|\nabla \cdot \mathbf{J}_B\|_2 \Delta p}{\|\mathbf{J}_B\|_2} \times 100\,(\%/\text{element})$$

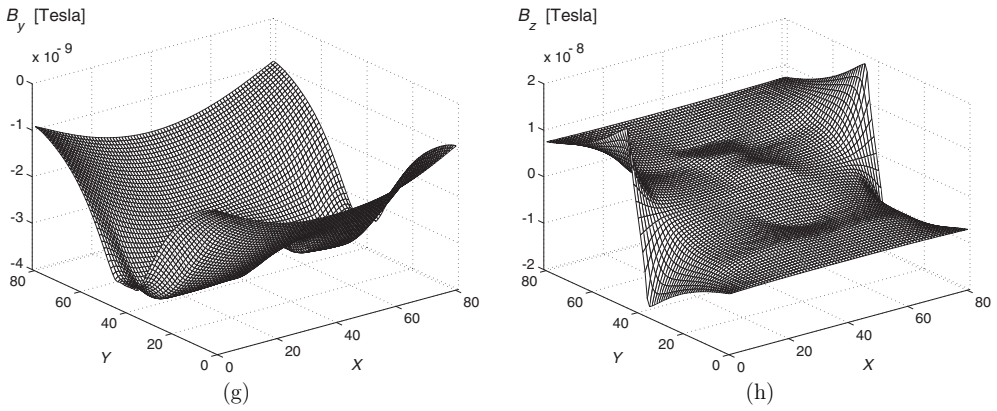

Figure 7. (Continued.)

where $\Delta p = 0.625$ mm is the size of each element. The computed values were $\varepsilon_{J_B} = 3.23 \times 10^{-2}\%$, $\varepsilon_{\nabla\cdot\mathbf{J}} = 1.0 \times 10^{-4}\%$/element and $\varepsilon_{\nabla\cdot\mathbf{J}_B} = 1.18 \times 10^{-4}\%$/element.

3.3. Typical numerical results using the thorax model

Figure 7(a) shows the resistivity distribution of the model in figure 5(d) within a region of $-5 < z < 5$ mm. The average resistivity value in figure 7(a) is 536 Ω cm. Resistivity values in the upper and lower regions of the model were 1072 and 268 Ω cm, respectively. The computed voltage V in (1) on the xy plane with $z = 2.5$ mm is shown in figure 7(b). Figures 7(c)–(h) show the computed current density and magnetic flux density on the same plane. Compatibility conditions were satisfied with $\varepsilon_{J_B} = 0.971\%$, $\varepsilon_{\nabla\cdot\mathbf{J}} = 0.725$ and $\varepsilon_{\nabla\cdot\mathbf{J}_B} = 0.94\%$/element.

3.4. Comparison with experimental results

For the model with narrow recessed electrodes in figure 5(e), the resistivity of the cylindrical object was 300 Ω cm. The resistivity of the background including two containers of recessed electrodes was 50 Ω cm. We performed the same computations as in the previous section and could obtain similar numerical results satisfying the compatibility conditions. Figures 8(a), (b) and (c) show the picture of the cubic phantom, magnitude image and phase image of the phantom on the axial imaging slice at the centre ($z = 0$). After processing the image including geometrical error correction and phase unwrapping, figure 8(d) shows the measured B_z obtained from the phase image in (c). The corresponding B_z computed from the three-dimensional forward solver is shown in figure 8(e). Figure 8(f) shows the error difference between the computed and the measured B_z. We define the relative L^2 error of the measured B_z as

$$\varepsilon_{B_z} = \frac{\left\| B_z - B_z^m \right\|_2}{\|B_z\|_2} \times 100\,(\%)$$

where B_z and B_z^m are computed and the measured magnetic flux densities, respectively. For the measured B_z in figure 8(d), $\varepsilon_{B_z} = 9.56\%$. If we excluded the outer most layer of 10 pixels (or elements) near the electrodes, $\varepsilon_{B_z} = 6.1\%$.

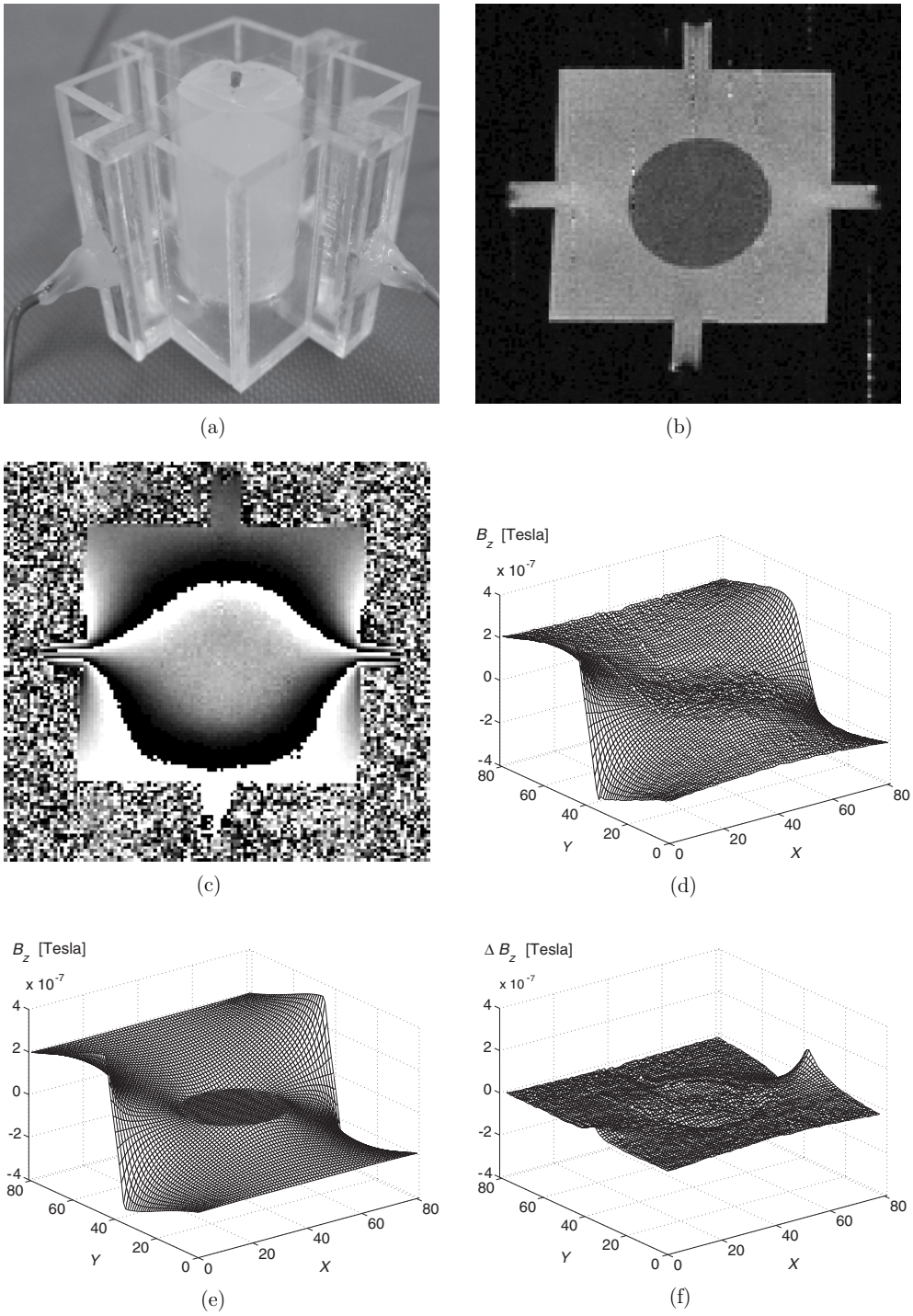

Figure 8. (a) Cubic phantom used in the experiment, (b) MR magnitude image of the phantom, (c) phase image at $z = 0$, (d) measured B_z at $z = 0$ and (e) computed B_z at $z = 0$ from the model with narrow recessed electrodes in figure 5(e). (f) The error difference between the computed and the measured B_z. The amount of injection current was 28 mA.

4. Discussion

Forward problem and image reconstructions in MREIT are inherently three dimensional. We also often need $\mathbf{B}$ or B_z from multiple imaging slices in resistivity image reconstructions. This means that we should use a three-dimensional forward solver. The forward solver should also provide much information on the design and verification of experimental procedures and results.

Numerical errors in the computed V and $\mathbf{B}$ are dependent on the resistivity distribution ρ of the model. We should expect a larger error when ρ changes more abruptly. Therefore, the errors ε_V and ε_B using the model in figure 5(b) might be smaller than the errors for the thorax model in figure 5(d). Considering the achievable minimal error of 0.1% in voltage measurements (Boone *et al* 1997), it would be better to use the mesh with $120 \times 120 \times 120$ elements for computing V. However, the error in measured $\mathbf{B}$ could be much larger than 0.1% (Scott *et al* 1992). Since measured $\mathbf{B}$ plays a more important role in most MREIT resistivity image reconstruction algorithms, we suggest using a mesh with fewer elements, for example, $80 \times 80 \times 80$ elements.

In developing a three-dimensional forward solver, we found that it is quite important to properly model electrodes and lead wires. Otherwise, the three-dimensional forward solver fails to produce correct numerical results satisfying the compatibility conditions in (7). This requires us to accurately compute $\mathbf{J}$ since $\mathbf{B}$ is calculated from $\mathbf{J}$. Higher current densities along edges of the electrodes must be computed correctly as shown in figures 7(c) and (d). In addition, we should not neglect the effect of a surface current on each copper electrode especially when the thickness of the recessed electrode is small.

When we compare the computed B_z with the measured one, we can see mostly random errors and two different kinds of systematic errors in figure 8(f). Random errors are mainly due to the random noise from the MRI scanner. One of the systematic errors occurs along the boundary of the cylindrical object. This is due to the difference in the resistivity value of the agar object immersed in the saline solution of the phantom compared with the resistivity value of the cylindrical object within the model in figure 5(e). We can observe the other kind of systematic errors in B_z near the electrodes. We believe this is mainly due to the difference in lead wire geometries between the phantom and the model in figure 5(e) since it was difficult to make the lead wires run perfectly straight in real experiments. To minimize this kind of systematic errors, we recommend using a lead wire guide fixed within the MRI scanner. This will be especially important for image reconstruction algorithms directly using the measured $\mathbf{B}$ or B_z without taking advantage of $\nabla^2 \mathbf{B}_{\mathcal{L}} = 0$ in $\mathcal{S}$.

One of the most common problems in a three-dimensional forward solver is the considerable computation times and storage requirements required to achieve a needed numerical accuracy. To reconstruct a resistivity image with a higher spatial resolution, we may need to use a finer mesh with an increased computation time. Our future study should contain different numerical techniques reducing the required computation time and storage requirement. Mesh generation for a subject with an irregular boundary shape is also nontrivial in three-dimensional problems. In MREIT, conventional MR images providing the structural information are always available. The forward solver in MREIT should, therefore, include a three-dimensional mesh generator utilizing this structural information.

5. Conclusion

For a given injection current through two recessed electrodes attached to the boundary of an electrically conducting subject, the three-dimensional forward solver described in this

paper computes voltage, current density and magnetic flux density distributions all within the volume conductor. Compared with analytic solutions and measured data, we found that its performance is good enough for applications in MREIT image reconstructions. The forward solver is also a valuable tool in the experimental design and validation.

Considering the experimental results using surface electrodes by Khang *et al* (2002) and Lee *et al* (2003), recessed electrodes should be used in our future experimental studies and, therefore, included in the forward solver. It is not yet clear what is the ultimate limit on the spatial resolution and accuracy of cross-sectional resistivity images in MREIT. For a presumably expected spatial resolution of 64×64 pixels with about 3×3 mm^2 pixel size, the computation time may not be a limiting factor unless real-time image reconstructions are required. However, depending on the application and reconstruction algorithm, it would be desirable to reduce the computation time of the forward solver using faster or multiple processors.

Currently, we utilize the forward solver in the development of new MREIT image reconstruction algorithms and their validations. It may also be used for the study of biomagnetism with a few modifications. Since some biological tissues are anisotropic in resistivity, future improvements should include a way to handle anisotropic material properties in addition to three-dimensional mesh generation techniques.

Acknowledgment

This work was supported by the grant R11-2002-103 from Korea Science and Engineering Foundation.

References

Awada K, Jackson D R, Williams J T, Wilton D R, Baumann S B and Papanicolaou A C 1997 Computational aspects of finite element modeling in EEG source localization *IEEE Trans. Biomed. Eng.* **44** 736–52

Birgul O, Eyuboglu B M and Ider Y Z 2003 Current constrained voltage scaled reconstruction (CCVSR) algorithm for MR-EIT and its performance with different probing current patterns *Phys. Med. Biol.* **48** 653–71

Birgul O, Ozbekl O, Eyuboglul B M and Ider Y Z 2001 Magnetic resonance conductivity imaging using 0.15 tesla MRI scanner *Proc. 23rd. Ann. Int. Conf. IEEE Eng. Med. Biol. Soc.*

Boone K, Barber D and Brown B 1997 Imaging with electricity: report of the European concerted action on impedance tomography *J. Med. Eng. Technol.* **21** 201–32

Burnett D S 1987 *Finite Element Analysis* (Reading, MA: Addison-Wesley)

de Munck J C, Faes T J C and Heethaar R M 2000 The boundary element method in the forward and inverse problem of electrical impedance tomography *IEEE Trans. Biomed. Eng.* **47** 792–800

Eyuboglu M, Birgul O and Ider Y Z 2001 A dual modality system for high resolution-true conductivity imaging *Proc. XI Int. Conf. Elec. Bioimpedance (ICEBI)* pp 409–13

Eyuboglu M, Reddy R and Leigh J S 1998 Imaging electrical current density using nuclear magnetic resonance *Elektrik* **6** 201–14

Gamba H R, Bayford D and Holder D 1999 Measurement of electrical current density distribution in a simple head phantom with magnetic resonance imaging *Phys. Med. Biol.* **44** 281–91

Gamba H R and Delpy D T 1998 Measurement of electrical current density distribution within the tissues of the head by magnetic resonance imaging *Med. Biol. Eng. Comput.* **36** 165–70

Gencer N G and Tanzer I O 1999a Forward problem solution of electromagnetic source imaging using a new BEM formulation with high-order elements *Phys. Med. Biol.* **44** 2275–87

Gencer N G and Tek M N 1999b Forward problem solution for electrical conductivity imaging via contactless measurements *Phys. Med. Biol.* **44** 927–40

Ider Z Y and Birgul O 1998 Use of the magnetic field generated by the internal distribution of injected currents for electrical impedance tomography (MR-EIT) *Elektrik* **6** 215–25

Ider Y Z, Onart S and Lionheart W R B 2003 Uniqueness and reconstruction in magnetic resonance electrical impedance tomography (MREIT) *Physiol. Meas.* **24** 591–604

Joy M L G, Lebedev V P and Gati J S 1999 Imaging of current density and current pathways in rabbit brain during transcranial electrostimulation *IEEE Trans. Biomed. Eng.* **46** 1139–49

Joy M L G, Scott G C and Henkelman R M 1989 *In vivo* detection of applied electric currents by magnetic resonance imaging *Magn. Reson. Imaging* **7** 89–94

Khang H S, Lee B I, Oh S H, Woo E J, Lee S Y, Cho M H, Kwon O, Yoon J R and Seo J K 2002 *J*-substitution algorithm in magnetic resonance electrical impedance tomography (MREIT): phantom experiments for static resistivity images *IEEE Trans. Med. Imaging* **21** 695–702

Kwon O, Lee J Y and Yoon J R 2002a Equipotential line method for magnetic resonance electrical impedance tomography (MREIT) *Inverse Problems* **18** 1089–100

Kwon O, Woo E J, Yoon J R and Seo J K 2002b Magnetic resonance electrical impedance tomography (MREIT): simulation study of *J*-substitution algorithm *IEEE Trans. Biomed. Eng.* **48** 160–7

Lee B I, Oh S H, Woo E J, Lee S Y, Cho M H, Kwon O, Seo J K and Baek W S 2003 Static resistivity image of a cubic saline phantom in magnetic resonance electrical impedance tomography (MREIT) *Physiol. Meas.* **24** 579–89

Mosher J C, Leahy R M and Lewis P S 1999 EEG and MEG: forward solutions for inverse methods *IEEE Trans. Biomed. Eng.* **46** 245–59

Polydorides N and Lionheart W R B 2002 A Matlab toolkit for three-dimensional electrical impedance tomography: a contribution to the Electrical Impedance and Diffuse Optical Reconstruction Software project *Meas. Sci. Technol.* **13** 1871–83

Pruis G W, Gilding B H and Peters M J 1993 A comparison of different numerical methods for solving the forward problem in EEG and MEG *Physiol. Meas.* **14** A1–A9

Saulnier G J, Blue R S, Newell J C, Isaacson D and Edic P M 2001 Electrical impedance tomography *IEEE Signal Process. Mag.* **18** 31–43

Scott G C, Joy M L G, Armstrong R L and Henkelman R M 1991 Measurement of nonuniform current density by magnetic resonance *IEEE Trans. Med. Imaging* **10** 362–74

Scott G C, Joy M L G, Armstrong R L and Hankelman R M 1992 Sensitivity of magnetic resonance current density imaging *J. Magn. Reson.* **97** 235–54

Seo J K, Yoon J R, Woo E J and Kwon O 2003a Reconstruction of current density distributions in axially symmetric cylindrical sections using one component of magnetic flux density: computer simulation study *Physiol. Meas.* **24** 565–77

Seo J K, Yoon J R, Woo E J and Kwon O 2003b Reconstruction of conductivity and current density images using only one component of magnetic field measurements *IEEE Trans. Biomed. Eng.* **50** at press

Vauhknonen P J, Vauhknonen M, Savolainen T andKaipio J P 1999 Three-dimensional electrical impedance tomography based on the complete electrode model *IEEE Trans. Biomed. Eng.* **46** 1150–60

Webster J G (ed) 1990 *Electrical Impedance Tomography* (Bristol: Adam Hilger)

Woo E J, Lee S Y and Mun C W 1994 Impedance tomography using internal current density distribution measured by nuclear magnetic resonance *Proc. SPIE* **2299** 377–85

Zhang N 1992 Electrical impedance tomography based on current density imaging *MS Thesis* University of Toronto, Canada